Highly and Adaptively Undersampling Pattern for Pulmonary Hyperpolarized ^{129}Xe Dynamic MRI

Sa Xiao, He Deng, Caohui Duan, Junshuai Xie, Haidong Li, Xianping Sun, Chaohui Ye, Xin Zhou

***Abstract*— Hyperpolarized (HP) gas (e.g., ^{3}He or ^{129}Xe) dynamic MRI could visualize the lung ventilation process, which provides characteristics regarding lung physiology and pathophysiology. Compressed sensing (CS) is generally used to increase the temporal resolution of such dynamic MRI. Nevertheless, the acceleration factor of CS is constant, which results in difficulties in precisely observing and/or measuring dynamic ventilation process due to bifurcating network structure of the lung. Here, an adaptive strategy is proposed to highly undersample pulmonary HP dynamic k-space data, according to the characteristics of both lung structure and gas motion. After that, a valid reconstruction algorithm is developed to reconstruct dynamic MR images, considering the low-rank, global sparsity, gas-inflow effects, and joint sparsity. Both the simulation and the in vivo results verify that the proposed approach outperforms the state-of-the-art methods both in qualitative and quantitative comparisons. In particular, the proposed method acquires 33 frames within 6.67 s (more than double the temporal resolution of the recently proposed strategy), and achieves high-image quality [the improvements are 29.63%, 3.19%, 2.08%, and 13.03% regarding the mean absolute error (MAE), structural similarity index (SSIM), quality index based on local variance (QILV), and contrast-to-noise ratio (CNR) comparisons]. This provides accurate structural and functional information for early detection of obstructive lung diseases.**

***Index Terms*— Highly and adaptively undersampling pattern (HUP), dynamic MRI, hyperpolarized ^{129}Xe, lung, compressed sensing (CS).**

Manuscript received September 21, 2018; revised November 9, 2018; accepted November 13, 2018. Date of publication November 20, 2018; date of current version May 1, 2019. This work was supported in part by the National Natural Science Foundation of China under Grant 81771917, Grant 81625011, Grant 81227902, and Grant 61471355, in part by the National Key R&D Program of China under Grant 2016YFC1304700, and in part by the Key Research Program of Frontier Sciences, CAS, under Grant QYZDY-SSW-SLH018. The work of X. Zhou was supported by the National Program for Support of Eminent Professionals (National Program for Support of Top-notch Young Professionals). *(Sa Xiao and He Deng contributed equally to this work.) (Corresponding author: Xin Zhou.)*

The authors are with the State Key Laboratory of Magnetic Resonance and Atomic and Molecular Physics, National Center for Magnetic Resonance in Wuhan, Wuhan Institute of Physics and Mathematics, Chinese Academy of Sciences - Wuhan National Laboratory for Optoelectronics, Wuhan 430071, China, and also with the University of Chinese Academy of Sciences, Beijing 100049, China (e-mail: xinzhou@wipm.ac.cn).

Color versions of one or more of the figures in this paper are available online at http://ieeexplore.ieee.org.

Digital Object Identifier 10.1109/TMI.2018.2882209

I. Introduction

MAGNETIC resonance imaging (MRI) has been widely used in the medical field because it provides images with high spatial resolution, good soft tissue contrast and no ionizing radiation. In particular, conventional MRI is based on the signal of proton. However, imaging of the lung is a challenge for the conventional MRI because the most area of the lung is air space where the density of proton is very low. Fortunately, hyperpolarized (HP) noble gas (such as ^{3}He and ^{129}Xe) MRI makes the MRI of lung air space feasible [1]–[3], which can offer the anatomical and physiological information of the lung, including the microstructure, gas-gas and gas-blood exchange functions [4]–[6]. HP gas MRI has revealed great potential in the early diagnosis of lung diseases, such as emphysema and chronic obstructive pulmonary disease (COPD) [3], [6].

Some pulmonary HP gas imaging techniques are developed to differentiate unhealthy from healthy lungs, which include the ventilation imaging [6], dissolved-phase ^{129}Xe imaging [4], and diffusion imaging [5]. Howbeit, the above do not visualize the dynamic ventilation process, which possibly conceals some abnormal regions, such as pulmonary air leaks and collateral ventilation [7], [8]. Accordingly, it makes sense to continuously image the lung during the respiration, denoted as pulmonary HP gas dynamic MRI. Such dynamic MRI can not only observe and measure the flow and diffusion of HP gases, but also acquire the anatomical and physiological information of the lung in various ventilation and dilated state [9]. This is helpful for the multiscale analysis with regard to the ventilation function of trachea and bronchial tree [9].

Although considerable progress has been made in dynamic HP gas MRI, it is still a challenge to simultaneously achieve good image quality and high temporal-spatial resolution owing to the non-renewable nature of HP magnetization. In 2000, Viallon *et al.* used the interleaved-spiral cine sequence to acquire HP dynamic images with good quality [10], but the temporal resolution was pseudo [9]. In 2001, Salerno *et al.* imaged the pulmonary ventilation process with high temporal resolution through the interleaved-spiral pulse sequences [11]. However, a large number of interleaves limited the image quality of HP gas MRI [12]. In 2003, Wild *et al.* successfully acquired dynamic images with high temporal and spatial resolution, but resulting in

radial streaking artifacts along the sampling trajectory [13]. Because compressed sensing (CS) is capable of accelerating the acquisition by undersampling raw data, it has been widely applied in MRI (termed as *CS-MRI*) [14]–[20]. In recent years, CS has also been successfully used in the dynamic MRI, such as the dynamic total variation [21], kernel-based low-rank [22] and low-rank plus sparse matrix decomposition (denoted as $L + S$) methods [23]. Moreover, CS is brought in pulmonary HP gas dynamic MRI [24], and 15 high-quality HP ^{129}Xe dynamic MR images are acquired during 6.67 seconds. However, the constant sampling ratio (SR) scheme is used in that case, which is not adaptive to the lung structure and gas motion property, generating some challenges in depicting HP gas flow and diffusion.

To achieve an adaptive strategy for pulmonary HP gas dynamic MRI, we consider the gas motion property in different anatomical areas of the lung. It is known that there are ∼24 levels in the bifurcating network of human lung, and the number of branches increases rapidly with the increasing of branching level [25], [26]. When HP gases are inhaled into the lung, they successively flow and diffuse through the branches. Since the lumen of trachea and bronchial tree (branching levels are 0-4) is patency (4.5 mm $\leq$ diameter $\leq$ 18 mm), the resistance for HP gas flow in this region is small and the gas flow rate is high. Consequently, it requires a fast imaging speed to depict the dynamic process of the gas flow while minimizing artifacts. Because this area has few branches, which results in few texture details and high transform-domain sparsity, we could utilize low SR (viz., high acceleration factor) to quickly sample k-space data according to the CS theory [27]–[30]. After that, when HP gases flow through the terminal bronchioli (branching levels are 5-16), the lumen is narrow (0.6 mm $\leq$ diameter $\leq$ 3.5 mm). The resistance for HP gas flow in this region is large and the flow rate is relatively low. Furthermore, the number of branches in this area increases rapidly and the sparsity decreases. This necessitates a high spatial resolution to preserve the high-frequency details of the lung. In this case, we should raise the SR (viz., low acceleration factor) to guarantee the image quality. At last, when the HP gases enter the acinar-airways (branching levels are 17-23), the transport of HP gas is primarily by diffusion due to the very narrow lumen (diameter $<$ 0.6 mm), and the gas motion further slows down [26]. It needs large SR to acquire abundant details of the lung. Since the spatial resolution of most HP gas MRI is larger than 1 mm [9], the motion of HP gas in this area has little effect on the image details. Thus, we keep the SR stable to visualize the ventilation process. Under these conditions, an adaptively undersampling pattern is introduced in this paper according to the characteristics of lung structure and gas motion.

After sampling HP k-space data under different SR values, an effective algorithm should be designed to reconstruct HP gas dynamic MR images. In [24], the reconstruction of dynamic images with an acceleration factor of 3 has been achieved by incorporating low-rank (L), sparse (S), and gas-inflow effects (G) constraints (denoted as $L+S+G$). Howbeit, this method is unsuitable to reconstruct images from the data obtained through the adaptively undersampling pattern because it does not take into account the different sparsity levels of each frame, and then cannot simultaneously suppress artifacts and preserve image details well.

With these considerations in mind, we construct a highly and adaptively undersampling pattern (HUP) for pulmonary HP ^{129}Xe dynamic MRI, containing an adaptively undersampling strategy and an effective reconstruction scheme. The adaptive strategy is to highly undersample HP dynamic k-space data, on the basis of the properties of both lung structure and gas motion. The scheme is to reconstruct pulmonary HP dynamic images from the undersampled data, considering the low-rank, global sparsity, gas-inflow effects, and joint sparsity. Simulation and *in vivo* results demonstrate that the proposed method displays a distinct superiority over some widely used baseline techniques. The contributions of this paper can be summarized as follows: 1) A novel adaptively undersampling scheme is proposed, which optimizes the SR of each frame based on the characteristics of pulmonary structure and gas motion. As a result, the temporal resolution is improved without obvious loss of image details. 2) A new reconstruction algorithm is designed by considering a joint sparsity term that constrains the different sparsity levels of each frame in the objective function. In this way, the artifacts are relieved and the structural details are preserved effectively in the reconstructed results.

The rest of this paper is organized as follows. In Section II, we briefly review some related works. In Section III, we explain the HUP-based pulmonary HP ^{129}Xe dynamic MRI method in details. In Section IV, we give extensive experimental results and discussions, and several factors of the proposed method are discussed in Section V. The conclusions and perspectives are given in Section VI.

II. Related Work

This section briefly reviews some related works, including the *CS-MRI*, $L + S$, and $L + S + G$ reconstruction algorithms.

A. CS-MRI Reconstruction

Compressed sensing can effectively reconstruct signals from undersampled data (far fewer samples than required by Nyquist sampling theorem) [27]–[30], and has been widely applied in MRI. There are three major conditions in *CS-MRI*. First, MR images should be sparse in a transform domain. Second, the artifacts in linear reconstruction caused by undersampling are incoherent, viz., the artifacts have a spatially noise-like structure. This can be satisfied via pseudo-random variable- density undersampling pattern. Third, a nonlinear way for reconstruction should be performed to enforce the sparsity using the L_1 norm [14]. Thus, an objective function could be

$$\min_{x} \|F_u x - y\|_2^2 + \lambda_1 \|\Psi x\|_1 + \lambda_2 \|x\|_{tv}, \tag{1}$$

where F_u is the undersampling Fourier encoding matrix, x is the reconstructed image, y is the undersampled data, Ψ is the sparsifying transform, tv is the total variation norm, and λ_1 and λ_2 are weighting parameters. The above optimization problem

can be solved by the iterative soft thresholding (ISTA) [31], nonlinear conjugate gradients [14], alternating direction method of multipliers (ADMM) [32], and so on. In HP gas MRI using CS, large flip angle can be used due to the undersampling pattern, thus improves the image quality [19].

B. $L+S$ Reconstruction

In the reconstruction of dynamic MRI, we should exploit the spatial-temporal correlations of the k-space data [21]–[24], [33], [34]. A feasible method is to consider the dynamic MR images as the superposition of background and dynamic components [23]. Owing to the low change speed, the background component can be characterized by low-rank in the time domain (called the L part). The dynamic component has a good sparsity in the sparse transformation domain due to separation with the background component (called the S part). Thereafter, the $L+S$ algorithm is to solve the following objective function,

$$\min_{L,S} \frac{1}{2} \|\mathrm{T}(L+S) - y\|_2^2 + \lambda_L \|L\|_* + \lambda_S \|\Psi S\|_1, \quad (2)$$

where T is the encoding or acquisition operator, L and S are the low-rank and sparse part of the images, λ_L and λ_S are the parameters to trade off the data consistency versus the nuclear norm and L_1 norm. This optimization problem can be solved using iterative soft thresholding of the singular values of L and of the entries of ΨS [23].

C. $L+S+G$ Reconstruction

The aforementioned $L+S$ algorithm is able to provide good quality of reconstruction results for dynamic MRI. However, it is difficult to directly use the $L+S$ method in HP gas dynamic MRI. When HP gas is inhaled into the lung, MR signals are affected by the gas-inflow effects (called the G part in [24]), which generates complex changes of signal intensity [35], [36]. These changes will bring negative factors in the sampling and reconstruction, and then degrade the image quality. To deal with this problem, the $L+S+G$ objective function is written as [24],

$$\min_{L,S} \left\{ \frac{1}{2} \|F_u(L+S) - y\|_2^2 + \lambda_G \|D(L+S) \circ (L+S)\|_2^2 + \lambda_L \|L\|_* + \lambda_S \|\Psi S\|_1 \right\}, \quad (3)$$

where D is the operator to acquire the differences between the adjacent frames, $\circ$ is the element-wise product operator, and λ_G, λ_L and λ_S are the regularization parameters to balance the gas- inflow effects, low-rank, and sparse part of the dynamic images, respectively. In particular, characteristics of dynamic images caused by the gas-inflow effects are constrained by the second term of the objective function. Similar to the $L+S$, Eq. (3) can be solved by the combination of singular value thresholding and iterative soft thresholding [23].

III. Adaptive Pulmonary HP ^{129}Xe Dynamic MRI

In this section, we introduce the HUP-based pulmonary HP ^{129}Xe dynamic MRI in details. This method exploits an adaptive strategy to optimize SR value of each frame, and designs a new objective function to reconstruct pulmonary HP ^{129}Xe dynamic MR images. It is good at improving the temporal resolution and quality of dynamic images.

A. Framework of HUP

The $L+S+G$ scheme in [24] adopts the constant SR scheme to undersample HP dynamic data. However, the scheme limits the acceleration factor in HP ^{129}Xe dynamic MRI because it does not adaptively take into account the different sparsity levels of each frame. To solve that problem, a novel pattern is designed to highly and adaptively undersample HP dynamic data, named as HUP. The framework of HUP is shown in Fig. 1, containing two major steps. One step is the adaptive strategy for highly undersampling dynamic k-space data. The SR of each frame is successively optimized according to the relationship between the reconstruction error and the SR value. This could take advantage of different sparsity levels of each frame, and then improve the temporal resolution and lessen motion artifacts of HP dynamic MRI. The other step is to reconstruct dynamic images, which utilizes a new objective function that takes into account low-rank, global sparsity, gas-inflow effects, and joint sparsity constraints. This ensures that each frame can be effectively reconstructed without serious artifacts and loss of details in some frames.

B. Adaptively Undersampling Strategy

Constant SR scheme is widely adopted in dynamic MRI [21]–[24]. Howbeit, when CS is used in pulmonary HP gas dynamic MRI, constant SR will lead to challenges in the exact depiction of HP gas flow and diffusion because of the specific structure of the lung. As mentioned in Section I, the details and transform- sparsity of the dynamic images will change when HP gases enter the branches in different levels. Moreover, the minimum of SR for exact reconstruction is proportional to the image transform-sparsity [27]–[30]. Thus, adaptive SR values should be used for each frame in the proposed undersampling scheme. This can be retrospectively achieved.

The adaptively undersampling scheme is designed as follows: First, we acquire fully sampled (FS) k-space data of HP ^{129}Xe dynamic MRI in the simulation experiments (the number of frames is M), and initialize the parameters such as Th (threshold of SR) and α [threshold of the mean absolute error (MAE)]. Then, the SR for the k-th frame is optimized according to reconstruction errors ($k = 1, \ldots, M$). Afterwards, undersampling patterns are obtained.

Specially, there are five steps in the optimization process of SR for the k-th frame:

1) Set SR = Th.

2) Generate variable-density undersampling patterns with the SR using Monte Carlo simulation, and then select the optimized pattern by minimizing the peak interference of transform point spread function [14].

3) Retrospectively undersample the k-space data.

4) Evaluate the reconstruction error of through the MAE.

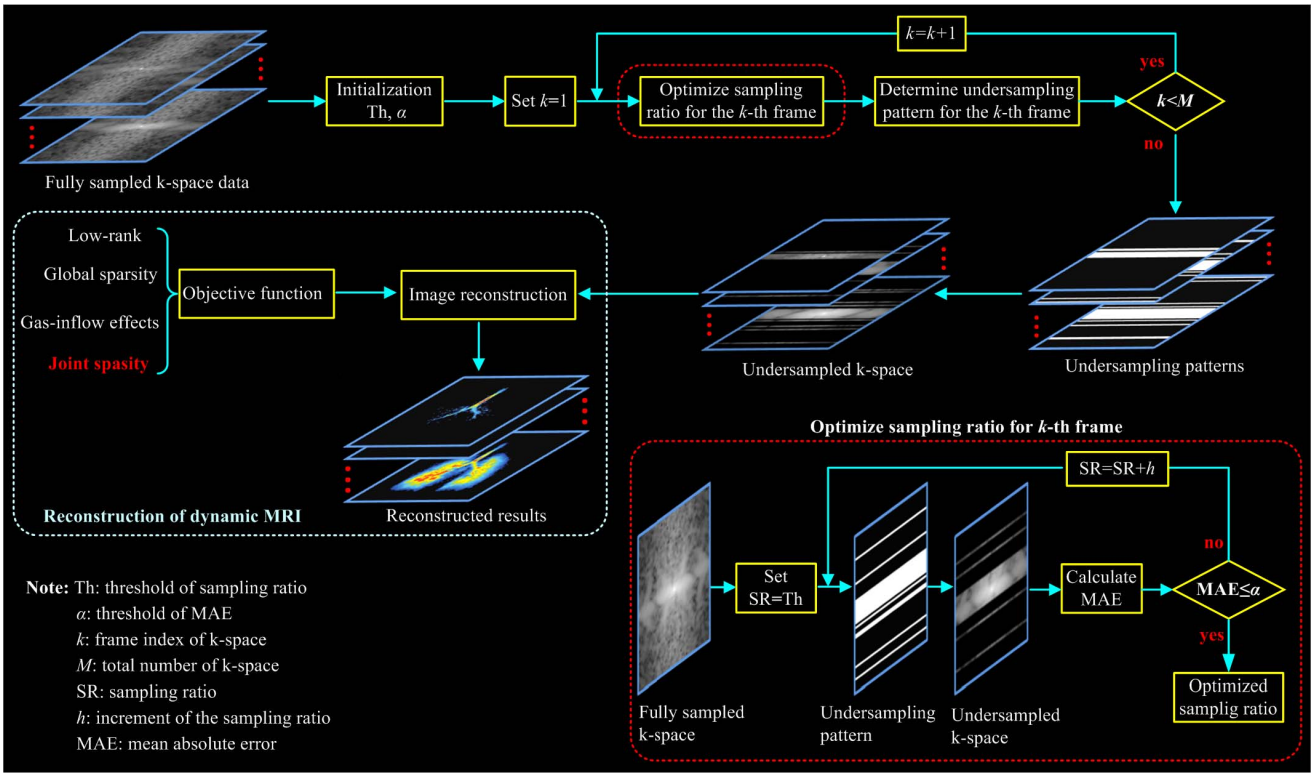

Fig. 1. Framework of the proposed pulmonary HP ^{129}Xe dynamic MRI, including two important steps. The first step is to adaptively undersample dynamic k-space data, and the second step is to effectively reconstruct dynamic images, considering the low-rank, global sparsity, gas-inflow effects, and joint sparsity constraints.

5) Determine whether the MAE is less than or equal to α. If not, increase SR with a fixed increment (h), that is, SR = SR + h and return to Step 2. If yes, the current SR is the optimized SR.

C. Reconstruction of Dynamic MRI

After the acquisition of undersampled data, it is important to effectively reconstruct dynamic images. We not only consider the global sparsity, low-rank and gas-inflow effects, but also incorporate the prior knowledge into the objective function, i.e., different sparsity levels of each frame that can be solved via the joint sparsity. The reconstruction function is,

$$\min_{L,S}\left\{\frac{1}{2}\left\|E(L+S)-d\right\|_2^2+\lambda_G\left\|D(L+S)\circ(L+S)\right\|_2^2 +\lambda_L\left\|L\right\|_*+\lambda_S\left\|\Psi S\right\|_1+\sum_{n=1}^{N}\lambda_n\left\|\Phi(L+S)_n\right\|_1\right\}, \quad (4)$$

where E is the transformation matrix of dynamic images to undersampled k-space data, L and S are the low-rank part and sparse part of the images, d is the undersampled k-space data, D represents the differences between the adjacent frames, $\circ$ is the element-wise product operator, Ψ is a global sparse transform matrix (such as the temporal Fourier transform or temporal total variation transform), Φ is the sparse transform matrix for each frame (such as wavelet transform or overcomplete dictionary), N is the number of frames, and λ_G, λ_L, λ_S, and λ_n are the regularization parameters to balance the gas-inflow effects, low-rank, global sparsity, and the joint sparsity of the images.

Specifically, the fifth term (joint sparsity) in Eq. (4) takes into account the different sparsity levels of each frame through various regularization parameters ($\lambda_1, \ldots, \lambda_N$). The parameters can be determined by solving following two equations: 1) $\lambda_1 + \lambda_2 + \ldots + \lambda_N = \lambda_D$, where λ_D is set in advance; 2) $\lambda_1 \mathrm{SR}_1 = \lambda_2 \mathrm{SR}_2 = \ldots = \lambda_N \mathrm{SR}_N$. According to the CS theory, the product of image sparsity ($||\Phi(L+S)_n||_1$) and the weighting coefficient (λ_n) has an effect on the reconstruction quality. When the product is too large, noise and artifacts can be suppressed, while losing some image details. Conversely, when the product is too small, the details are preserved, but the noise and artifacts are obvious. Accordingly, the regularization parameters (viz., $\lambda_1, \ldots, \lambda_N$) are set based on the above, aiming to effectively preserve details and suppress artifacts and noise.

In this paper, we adopt the combination of singular value thresholding and iterative soft thresholding [23] to solve Eq. (4) because it has a good convergence and can guarantee optimal solutions of the L and S. Regularization parameters λ_G, λ_L, λ_S, and λ_D are empirically chosen based on visual inspection, which leads to good results [23], [24]. The iterations are terminated when the relative change in the solution is less than 10^{-5}.

D. In Vivo HUP

The optimization of each SR in Section III. B is based on the pre-existing FS data, and can be applied easily in the

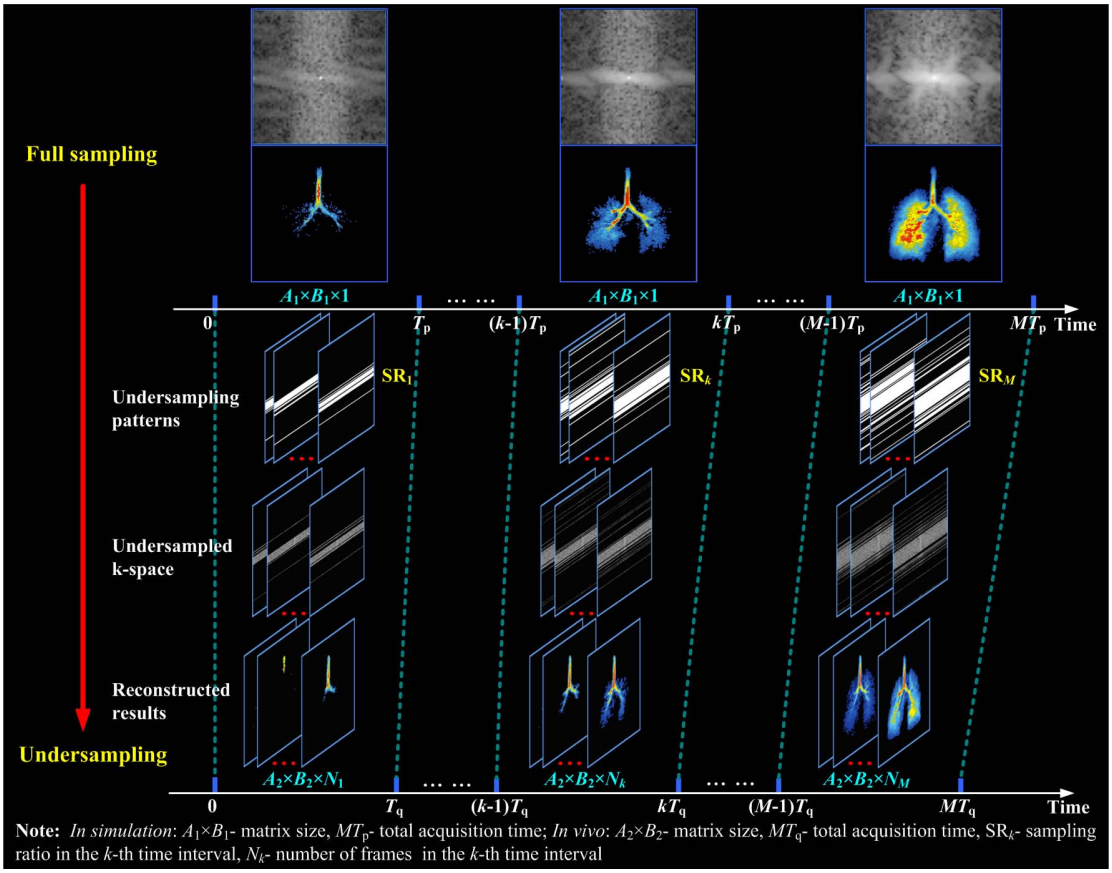

Fig. 2. Flowchart of *in vivo* HUP. According to the results acquired in the simulation experiments (fully sampling), optimal undersampling patterns are determined in the *in vivo* experiments.

simulation experiments through retrospective undersampling. However, in *in vivo* experiments, the imaging parameters may be different from those in simulation. It is hard to directly apply the optimized SR values in that case. Hence, we need to design the adaptively undersampling pattern according to the imaging parameters in actual experiments. Fig. 2 illustrates how we design the adaptively undersampling pattern in *in vivo* experiments. The first column in Fig. 2 represents the full sampling results of simulation experiments, where A_1, B_1 and M denote the number of phase encoding, frequency encoding and frames, and T_p denotes the acquisition time of one frame (e.g., $A_1 = B_1 = 64$, $M = 15$, $T_\mathrm{p} = 0.672$ s). The second column represents the undersampling results of the *in vivo* experiments, where A_2 and B_2denote the number of phase encoding and frequency encoding, SR_k denotes the optimized SR for the k-th frame, MT_q represents the total acquisition time, and N_k stands for the number of frames in the k-th time interval, respectively (e.g., $A_2 = B_2 = 128$, $N_1 + N_2 + \ldots + N_M = 33$, $MT_\mathrm{q} = 6.67$ s).

The concrete steps for acquiring the undersampling scheme in *in vivo* experiments are as follows:

First, according to the imaging parameters acquired in the simulation experiments, we determine the time period of each frame. For example, the time period of the k-th frame is from $(k-1)T_\mathrm{p}$ to kT_p. In this way, we obtain proper SR corresponding to each period, which is prior optimized in Section III. B.

Second, we search for the time period and the corresponding number of frames in *in vivo* experiments. Assume that the HP gas flow rate in the lung is proportional to the inhalation rate, and the volume of inhaled gas during each period in simulation experiments is equal to that during each period in *in vivo* experiments (i.e., $r_1 T_\mathrm{p} = r_2 T_\mathrm{q}$, where r_1 and r_2 denote inhalation rate of gas in the simulation and *in vivo* experiments). We use the SR_k in the k-th time period in *in vivo* experiments. Therefore, the acquisition time of one undersampled frame (T_k) in this period can be acquired according to the number of phase encoding and SR_k, viz., $T_k = (A_2/A_1 \times \mathrm{SR}_k) \times T_\mathrm{p}$. Hence, the number of frames in the k-th period is T_q/T_k. It should be noted that the number of frames in each period is an integer, which possibly needs to be adjusted properly.

Finally, we generate the adaptively undersampling patterns, and then undersample HP dynamic k-space data.

After that, pulmonary HP dynamic images are reconstructed through the reconstruction scheme introduced in Section III. C.

IV. Experimental Results

In this section, we first introduce the simulation and *in vivo* data and baseline methods for comparison. After that, we use experimental results to test the effectiveness and practicality of the proposed scheme.

A. Data and Baseline Methods

Informed consents were obtained from all volunteers (seven healthy subjects). All experiments were performed according to the guidelines and regulations provided and approved by the Institutional Review Board of Wuhan Institute of Physics and Mathematics (WIPM), Chinese Academy of Sciences (CAS).

The experiments were performed on a 1.5 Tesla whole-body MRI scanner (Avanto, Siemens). Enriched xenon was polarized through the spin-exchange optical pumping technique [37] with a "freeze-out" accumulation procedure using a cold finger and home-built xenon polarizer. Volumes of 500 mL HP ^{129}Xe were collected in a Tedlar bag, and the available polarization of ^{129}Xe was approximately 20%. All subjects were trained to breathe in HP gas from their functional residual capacity at a constant rate (50-100 mL s^{-1}).

Simulation experiments were implemented on two subjects with a home-built transmit-receive vest RF coil. A variable flip angle (VFA) scheme [24] was used here because it could effectively compensate for the decay of HP magnetization during the data acquisition process, thus maintained the SNR and preserved the details of dynamic images (For example, if the excitation number was 626, the initial flip angle was 3° and the last one was 90°). Then we fully acquired pulmonary HP ^{129}Xe dynamic data, where imaging parameters were: 2D FLASH sequence, centric encoding, matrix size = 64 × 64, initial flip angle $\theta_1 = 3°$, slice thickness = 20 cm, frame number = 15, echo time = 5.0 ms, time of repetition = 10.5 ms, field of view = 384 mm × 384 mm, bandwidth = 10.24 kHz. After that, the HUP-based adaptively undersampling patterns were generated from the FS data of one volunteer. Here, we set the parameter Th = 0.10 in Fig. 1. If SR was smaller than 0.10, the number of encoding lines acquired would be very small for the resolution (images of 128 × 128 or 64 × 64), which was not acceptable [5]. The α was set to 0.01 because the reconstruction would be considered as a good result if the MAE was less than 0.01 [19]. As for the h, it was set to 0.02 since it was the minimum increment when h was accurate to two decimal places. Afterwards, we used the acquired HUP-based undersampling patterns to retrospectively undersample the FS data of another volunteer. The reconstruction performance was measured by the MAE, structural similarity index (SSIM) [38], quality index based on local variance (QILV) [39], and contrast-to-noise ratio (CNR). Among them, MAE provided an absolute error measure, SSIM estimated the structure missing, QILV indicated some blurring, and CNR gave the quality of the contrast.

Five healthy volunteers were enrolled for HP ^{129}Xe dynamic MRI *in vivo* experiments. The imaging parameters were: matrix size = 128 × 128, initial flip angle $\theta_1 = 2.43°$, and the other parameters were the same as those in the simulation experiment. Then, we achieved adaptively undersampling patterns for prospectively undersampling HP dynamic k-space data. Then, HP ^{129}Xe MR images were reconstructed through the $L + S$ [23], $L + S + G$ [24], and the proposed HUP algorithms. Since the MAE, SSIM and QILV were reference measures which were not available in the *in vivo* experiments, we adopted the CNR to evaluate the image quality.

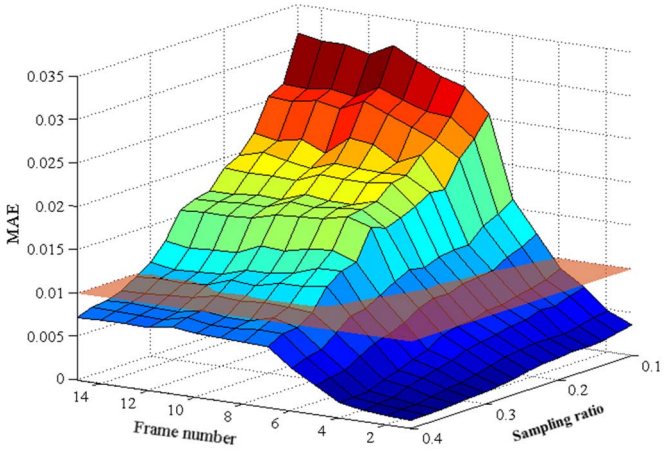

Fig. 3. The relationship among the MAE, sampling ratio, and frame number. The vertical axis is the reconstruction error (MAE), and the orange plane is the threshold of MAE ($\alpha = 0.01$).

To evaluate the performance of the proposed reconstruction algorithm, we selected $L+S$ and $L+S+G$ as baseline methods for comparison. Since the baseline methods were unsuitable for the variable SR scheme, we generated the undersampling patterns with constant SR (SR = 34%) for reconstruction. A two-tailed Student's t-test was performed for statistical comparison of quantitative metrics (e.g., MAE, SSIM, QILV, or CNR), and a P-value < 0.05 was considered as statistically significant. All groups of MR data were processed in MATLAB (MathWorks, Natick, MA).

B. Simulation

Fig. 3 displays the MAE values under different sampling ratios and frame indexes. We adopt the *CS-MRI* reconstruction [14] in this case. If the threshold of MAE is set to 0.01 (viz., $\alpha = 0.01$), we can get the optimized SR for the 15 frames: 0.10, 0.10, 0.10, 0.10, 0.12, 0.20, 0.28, 0.30, 0.30, 0.32, 0.34, 0.34, 0.34, 0.34, and 0.34, respectively.

Fig. 4 shows the 2nd, 6th, and 15th frames of FS images and corresponding reconstructed results achieved using the $L + S$, $L + S + G$ and HUP algorithms, where the white rectangles denote the blurring and loss of details, and the white circles denote the artifacts and noise. In particular, $L + S$ and $L + S + G$ are used to reconstruct the images with the SR = 34%, and HUP is with the optimized SR. The SR values in Fig. 4(d1)-(d3) are 10%, 20% and 30%, respectively. We can find that the reconstructed result of the 2nd frame through HUP has little reconstruction errors [see Fig. 4(d1)], similar to those obtained using the $L + S$ and $L + S + G$ [see Fig. 4(b1) and (c1)]. This demonstrates that the proposed HUP strategy is feasible when the acceleration factor is high. For the results of the 6th frame, both $L + S + G$ and HUP algorithms have good performance in terms of artifacts and noise [as shown in Fig. 4(c2) and (d2)]. However, considerable artifacts and blurring are found in Fig. 4(b2). As for the results of the 15th frame, obvious reconstruction errors (denoted by the white rectangles) can be found in Fig. 4(b3). The $L+S+G$ has a better performance than $L+S$, but losing some image details [see Fig. 4(c3)]. Nevertheless, image details are preserved well, and noise and artifacts are effectively

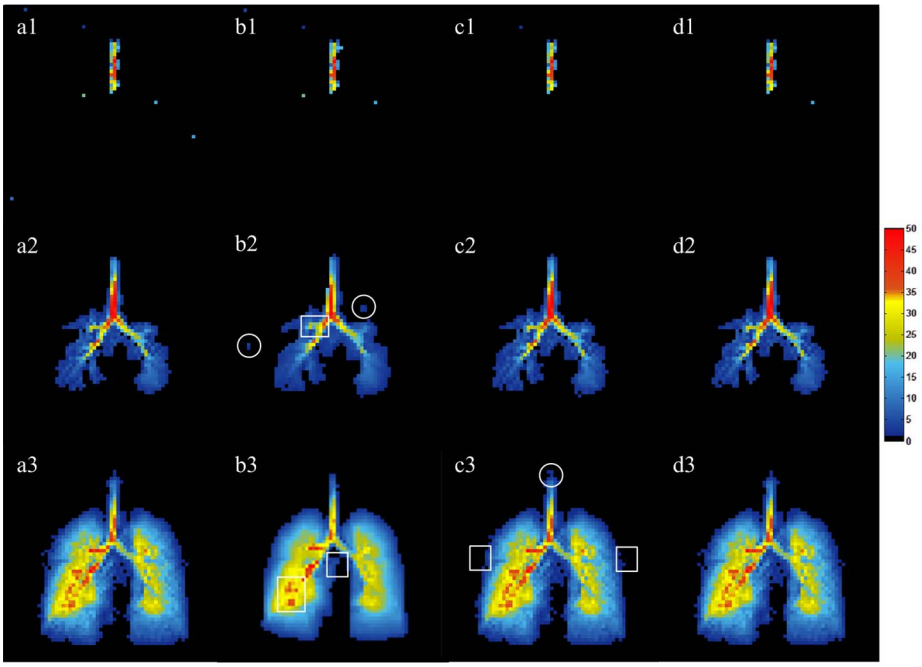

Fig. 4. Reconstructed results of the 2nd, 6th, and 15th frames obtained using different algorithms. (a1)-(a3) Reconstructed results through FFT from the fully sampled data. For the undersampled data, reconstructed results are obtained using the $L+S$ (b1)-(b3), $L+S+G$ (c1)-(c3) and HUP schemes (d1)-(d3), respectively.

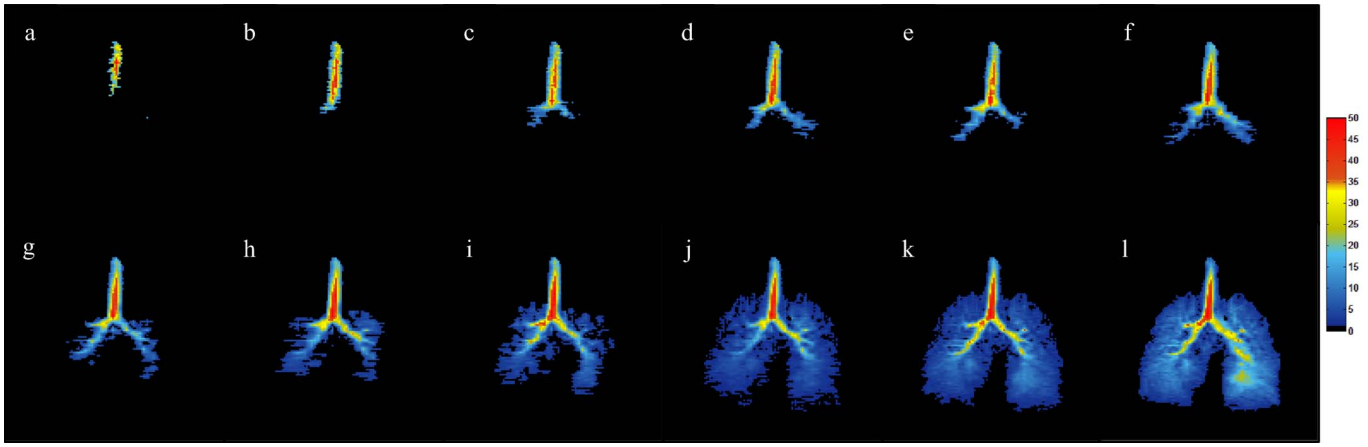

Fig. 5. For a healthy volunteer, twelve representative frames of *in vivo* HP ^{129}Xe dynamic MR images are achieved using the proposed HUP method. (a-l) The 3rd, 6th, 9th, 12th, 15th, 18th, 21st, 23rd, 25th, 27th, 29th, and 31st frames.

mitigated in Fig. 4(d3). Fig. 4 indicates that the HUP method outperforms the baseline methods in retrospective experiments.

Table I lists the MAE, SSIM, QILV, and CNR of the results through different methods in retrospective experiments. In term of MAE and CNR, the HUP has statistically significant improvement when compared with the $L+S$ and $L+S+G$. Moreover, the HUP can improve the SSIM and QILV of reconstructed images in a statistical sense when compared with the $L+S$. These statistical characteristics are unfounded for the comparisons between the HUP and $L+S+G$.

C. In Vivo

In *in vivo* experiments, a total of 33 frames are sampled in 6.67 s and the corresponding SR values are: 0.10, 0.12, 0.12, 0.12, 0.12, 0.20, 0.20, 0.20, 0.28, 0.28, 0.30, 0.30, 0.30, and 0.32, respectively.

Fig. 5 displays twelve representative frames of dynamic pulmonary inspiration images of a healthy volunteer acquired using the proposed HUP scheme. We can find that the filling of HP gases from the trachea to the bronchi and acinar-airways is effectively visualized with high temporal and spatial resolution. In this way, a good visualization of HP ^{129}Xe flow/diffusion is provided with the acceleration factor of 3-10, and then dynamic ventilation process can be effectively observed within 6.67 s.

Fig. 6 shows the representative reconstructed results (10th, 20th, 25th, 27th, 30th, and 32nd frames) obtained using the $L+S$, $L+S+G$, and HUP. The corresponding SR values are 0.10, 0.10, 0.20, 0.20, 0.30, and 0.30, respectively. It can

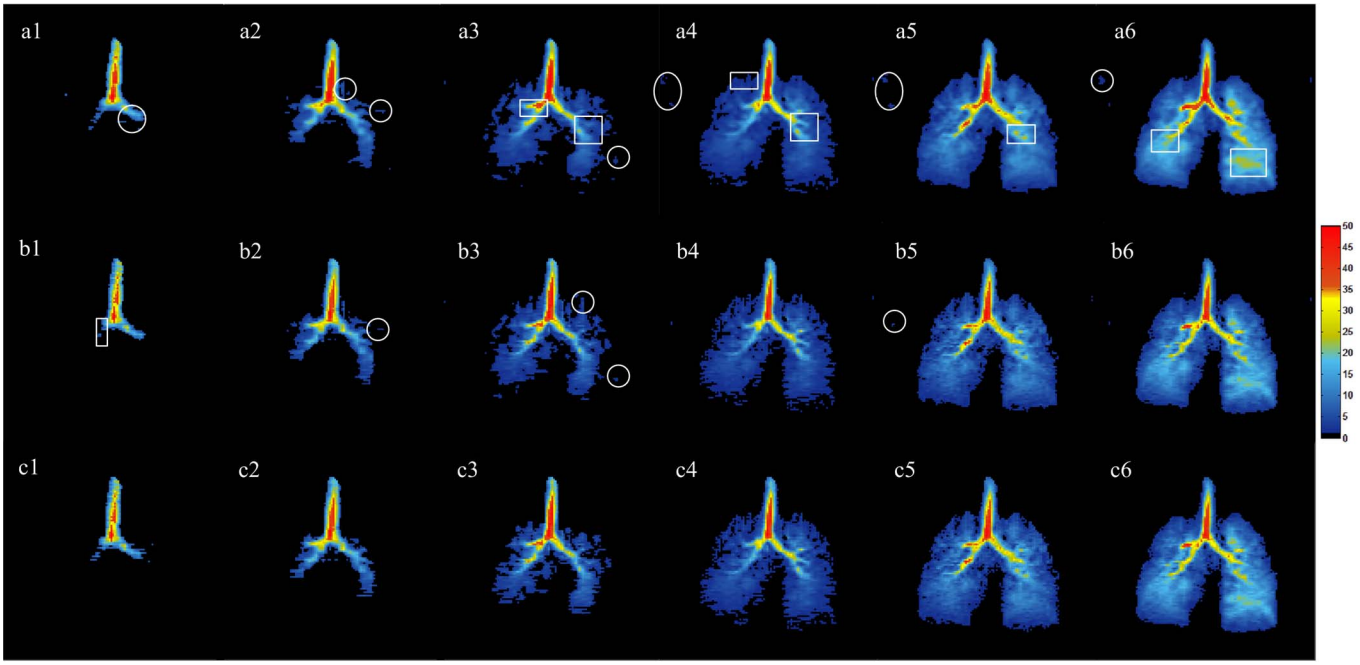

Fig. 6. The 10th, 20th, 25th, 27th, 30th, and 32nd frames of *in vivo* HP ^{129}Xe dynamic MR images through different algorithms. (a1)-(a6), (b1)-(b6), and (c1)-(c6) denote the reconstructed results obtained using the $L+S$, $L+S+G$, and HUP algorithms, respectively.

TABLE I
COMPARISONS OF THE MAE, SSIM, QILV AND CNR IN SIMULATION EXPERIMENTS OBTAINED USING DIFFERENT ALGORITHMS

	MAE (%)	SSIM	QILV	CNR
L+S	1.94±0.92	0.77±0.06	0.91±0.09	23.97±1.25
L+S+G	1.35±0.96	0.94±0.09	0.96±0.02	31.15±4.10
HUP	0.95±0.93	0.97±0.03	0.98±0.03	35.21±6.06
P_1	< 0.001	< 0.001	< 0.001	< 0.001
I_1	51.03%	25.97%	7.69%	46.89%
P_2	0.045	0.199	0.062	0.003
I_2	29.63%	3.19%	2.08%	13.03%

where P_1 and I_1 denote the P-value and improvement when the results through the HUP are compared with those obtained using the L+S, and P_2 and I_2 denote the P-value and improvement when the results through the HUP are compared with those obtained using the L+S+G.

TABLE II
COMPARISONS OF CNR VALUES OBTAINED USING THE $L+S$, $L+S+G$ AND HUP ALGORITHMS FOR *In Vivo* EXPERIMENTS

No.	1	2	3	4	5
L+S	29.9±8.2	37.3±12.6	31.7±7.7	31.7±11.4	30.7±6.6
L+S+G	33.3±8.4	42.5±14.5	35.5±8.0	35.0±13.1	36.3±10.7
HUP	43.7±11.6	52.4±13.5	46.9±11.8	49.4±14.5	47.2±12.5
P_1	< 0.001	< 0.001	< 0.001	< 0.001	< 0.001
I_1	46.43%	40.65%	48.14%	56.05%	53.68%
P_2	< 0.001	< 0.001	< 0.001	< 0.001	< 0.001
I_2	31.55%	23.43%	32.26%	46.78%	30.25%

where P_1 and I_1 denote the P-value and improvement when the results through the HUP are compared with those obtained using the L+S, and P_2 and I_2 denote the P-value and improvement when the results through the HUP are compared with those obtained using the L+S+G.

be seen that there are some obvious artifacts and blurring in Fig. 6(a1)-(a6) and (b1)-(b5), where artifacts and noise are indicated by the white circles and the blurring is indicated by the rectangles. In the corresponding results obtained using HUP, these artifacts and blurring are significantly relieved and image details are preserved effectively [see Fig. 6(c1)-(c6)].

Table II lists CNR values obtained using the $L+S$, $L+S+G$ and HUP algorithms. We can find that the HUP has statistically significant improvements (the minimum is 23.43% while the maximum is 56.05%) when compared with the $L+S$ ($P < 0.001$) and $L+S+G$ ($P < 0.001$). These results further demonstrate the effectiveness of HUP in prospective experiments.

Fig. 7 shows signal-frame curves from regions of interest (ROI) of mid zones of the left lung (ROI-L), right lung (ROI-R), and the trachea (ROI-T). It can be noticed the curves of ROI-L and ROI-R have a similar trend of variation. The amplitude of ROI-T curve is higher than that of other

TABLE III
SPEARMAN'S RHO VALUES THAT MEASURE THE CORRELATIONS BETWEEN THE SIGNAL-FRAME CURVES OF ROI-L AND ROI-R IN FIVE HEALTHY SUBJECTS

Subject No.	1	2	3	4	5
R[a]	0.998	0.976	0.965	0.984	0.951

[a]Spearman's Rho Values

ROIs, and can reach a steady state in a short time. Afterwards, the Spearman's rho values are calculated to assess the correlations between the signal-frame curves of ROI-L and ROI-R, as shown in Table III. It can be seen that there exists a strong correlation between the curves of ROI-L and ROI-R for all healthy subjects. The above features of the signal-frame curves are in accordance with the related works [24], [36].

D. Motion Estimation

After acquiring the pulmonary HP ^{129}Xe dynamic images, we adopt a widely used motion field estimation technique [40]

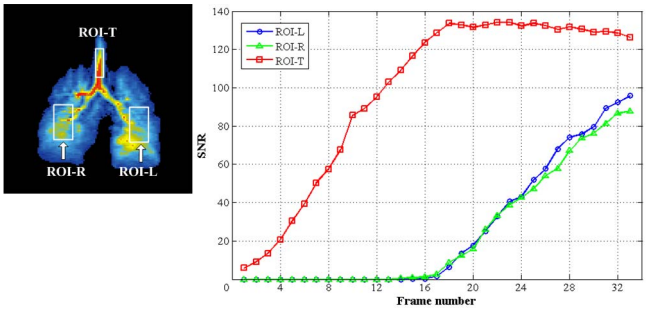

Fig. 7. Signal-frame curves of ROIs from the left lung (ROI-L), right lung (ROI-R) and trachea (ROI-T).

to estimate the motion of HP ^{129}Xe. In this case, the pulmonary ventilation function at different stages of inspiration could be analyzed. Fig. 8(a)-(c) shows the flow field of HP ^{129}Xe in the 10th, 20th and 30th frames of dynamic images. The ROIs (main bronchus, secondary bronchi, and acinar-airways region) are resized (indicated by the green rectangles). We can find that the results can roughly depict the flow/diffusion properties of the HP ^{129}Xe. Specially, some conclusions are drawn: 1) The velocities of HP gas flow or diffusion in the trachea and main bronchus are higher than those in other areas, which is consistent with the gas motion characteristics in the lung; 2) The direction of gas motion is reasonable (gas moves from the center to the periphery of the lung). Similar features are also observed in results of other four volunteers.

We compare the obtained motion field (the inspiratory flow rate is 50-100 ml s^{-1} in this paper) with the related work [41] (the inspiratory flow rate is 150-200 ml s^{-1}). In Fig. 8(a)-(b), the velocities of HP ^{129}Xe in the main bronchus, secondary bronchi region are 9.8±5.3 cm s^{-1} and 6.8±0.9 cm s^{-1}. According to [41], the gas flow velocities are approximately 25 cm s^{-1} and 15 cm s^{-1} in the corresponding region. Assume that the gas flow velocity in the lung is proportional to the inspiratory flow rate, the results in this paper are in good agreement with those in [41]. In this way, the gas motion field could be availably estimated. In Fig. 8(c), the velocity in the acinar-airways region is about 1.5±0.6 cm s^{-1}, which has not been directly measured by other works. Therefore, the acquired velocity in acinar-airways needs to be validated in the future.

According to the gas flow velocities measured in [41] and the geometric and dimensional model of human lung in [25], it can be found that the length from the main trachea to the secondary bronchi is about 19 cm, and the gas motion velocity in this area is about 22 cm s^{-1}. Therefore, the motion time of HP ^{129}Xe from the main trachea to secondary bronchi is about 0.9 s. Under the assumption, the corresponding time is about 2.0 s if inspiratory flow rate is 50-100 ml s^{-1}, which is consistent with the motion time measured in this paper. In the *in vivo* experiments, we use low SR values (0.10-0.12) in the period of 0-2.2 s because the image details in this period are few and the transform-sparsity is high (HP ^{129}Xe move from the main trachea to the bronchioli). After that, we augment the SR (0.12-0.30) in the period of 2.2- 5.6 s because the image details are increasing rapidly (from the bronchioli to acinar-airways). Last, we keep the SR stable (0.30 -0.32) within the

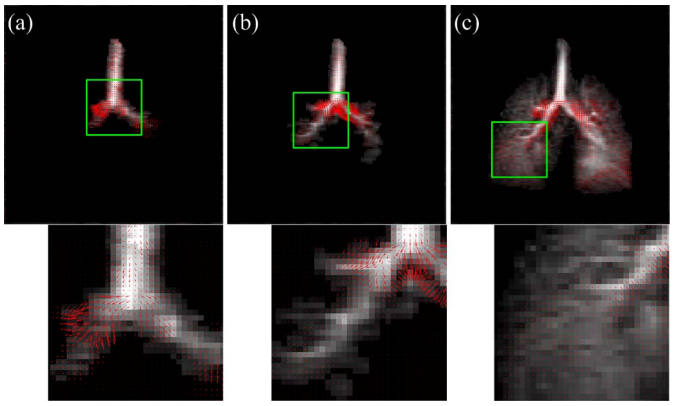

Fig. 8. The flow fields of HP ^{129}Xe in the 10th (a), 20th (b) and 30th (c) frames of dynamic images. The resized ROIs (indicated by the green rectangles) are displayed in the lower column, where red arrows denote the direction and magnitude of gas motion fields.

time period of 5.6-6.7 s because the image details almost stop increasing (in acinar-airways). This verifies the right analysis of properties of the pulmonary structure and gas motion in Section III. B, and demonstrates the rationality of the proposed HUP scheme. Since the gas flow velocities in the small airways are not measured in [41], the motion of HP ^{129}Xe in these places should be verified in the future.

V. Discussions

In this section, we discuss some factors of the proposed HUP scheme, e.g. the undersampling pattern, reconstruction strategy, motion estimation, and some limitations.

A. Undersampling Pattern

In this paper, a highly and adaptively undersampling scheme is proposed to improve the performance of HP ^{129}Xe dynamic MRI. The experimental results show that the acceleration factor can be reached to 3-10, while achieving pulmonary HP ^{129}Xe dynamic images with high temporal and good spatial resolution. When compared with other HP ^{129}Xe dynamic MRI [24], [36], the temporal resolution of dynamic MRI through the proposed HUP is more than double under the same spatial resolution of 3 mm. This is helpful for accurately observing lung ventilation. Furthermore, low-rank properties are boosted with the increase of the continuity and the total number of frames [22], which can improve the reconstruction quality. High temporal resolution is able to promote the accuracy of gas motion field as well.

In the SR optimization process, we use MAE to evaluate the reconstruction error, which is used to judge whether an exact reconstruction is obtained from undersampled data. We could also select other evaluation indexes as needed, such as the root mean square error (RMSE), SSIM, mean structural similarity index (MSSIM), QILV. This increases the flexibility of the proposed undersampling pattern. As for the threshold of the evaluation index, it is a feasible approach to select the α by combining some related works [17]–[19] with the visual effects of reconstruction results under different SR values.

B. Objective Function

The objective function is the key ingredient in the image reconstruction. In *in vivo* experiments, obvious artifacts and loss of structure are observed in the reconstruction results using the $L + S$ and $L + S + G$ (especially under the low SR values). This indicates that the objective functions of the baseline methods are unsuitable for the variable SR scheme. By considering the different sparsity levels of each frame, the provided objective function in HUP can effectively solve the challenge caused by the variable SR. Then, dynamic images with high quality are reconstructed.

Proper weighting coefficients of transform-sparsity of each frame are vital in the joint sparsity term in Eq. (4). Too large (or small) weighting coefficients possibly result in some negative effects in the reconstruction results [17]. Specially, the products of the transform-sparsity of different frames (viz., $||\Phi(L+S)_n||_1$) and weighting coefficients (viz., λ_n) represent the importance of each frame in the joint sparsity term. To balance the importance, those products are assumed to be the same. Since the minimum SR value for exact reconstruction is proportional to the image transform-sparsity [27]-[30], the assumption becomes: $\lambda_1 \mathrm{SR}_1 = \lambda_2 \mathrm{SR}_2 = \ldots = \lambda_N \mathrm{SR}_N$. This provides a concise way to acquire the proper weighting coefficients, and the efficiency is validated by the experimental results.

C. Motion of HP ^{129}Xe

After obtaining pulmonary HP ^{129}Xe dynamic images, the gas motion field (including the motion velocity and direction of HP ^{129}Xe) is used to analyze the gas motion pattern in the lung during the inspiration. This provides a beneficial supplement to the *in vivo* measurement of gas flow in human airways in [41]. Accordingly, pulmonary gas distribution is investigated during the inspiration process, and then the pulmonary structure and function will be evaluated. This is helpful for the clinical diagnosis and research of some lung diseases. Nevertheless, it needs to be noted that there are some unreasonable places in the motion field. For example, the velocities of HP ^{129}Xe are improper in the region which has few changes of signal intensities [e.g. the trachea area in Fig. 8(b)]. Therefore, the obtained motion field of HP ^{129}Xe needs further improvements.

D. Limitations

Our study has some limitations. First, both the temporal and spatial resolution of the simulation experiments under the full sampling condition are lower than that of the *in vivo* experiments under the undersampling condition. To maintain the effectiveness of the simulation, matrix size in the simulation is set to 64×64 for the trade-off between temporal and spatial resolution. Second, the undersampling patterns are designed according to the characteristics of gas motion and pulmonary structure, which may be unsuitable for the dynamic MRI of other parts of human body. Therefore, the feasibility of HUP should be further explored. Third, constant inspiratory flow rate is achieved by the valid training of subjects in this paper. This requires good coordination for subjects in the inhalation speed control. In the future study, a human ventilator should be built to control the inhalation speed and synchronization, which can increase the stability and efficiency of the experiments.

VI. Conclusions

To improve both the temporal resolution and image quality of pulmonary HP ^{129}Xe dynamic MRI, we present a highly and adaptively undersampling pattern in this paper. The presented method uses an adaptively scheme to undersample k-space data that optimizes the SR of each frame, followed by an effective reconstruction strategy to guarantee good quality of pulmonary dynamic images. Both the simulation and *in vivo* results have demonstrated the feasibility of the proposed method. Compared with several baseline methods, the presented method not only acquires more frames within the same scanning time, but also yields fewer artifacts and noise while preserving fine details. This will provide more information about the pulmonary structure and function. In the future, more researches should be paid attention to in analyzing physiology and pathophysiology of different obstructive lung diseases.

References

[1] M. S. Albert *et al.*, "Biological magnetic resonance imaging using laser-polarized ^{129}Xe," *Nature*, vol. 370, no. 6486, pp. 199–201, Jul. 1994.

[2] H. Deng *et al.*, "Constant-variable flip angles for hyperpolarized media MRI," *J. Magn. Reson.*, vol. 263, pp. 92–100, Feb. 2016.

[3] F. C. Horn *et al.*, "Regional ventilation changes in the lung: Treatment response mapping by using hyperpolarized gas MR imaging as a quantitative biomarker," *Radiology*, vol. 284, no. 3, pp. 854–861, Sep. 2017.

[4] B. Driehuys, G. P. Cofer, J. Pollaro, J. B. Mackel, L. W. Hedlund, and G. A. Johnson, "Imaging alveolar–capillary gas transfer using hyperpolarized ^{129}Xe MRI," *Proc. Nat. Acad. Sci. USA*, vol. 103, no. 48, pp. 18278–18283, Nov. 2006.

[5] J. F. P. J. Abascal, M. Desco, and J. Parra-Robles, "Incorporation of prior knowledge of signal behavior into the reconstruction to accelerate the acquisition of diffusion MRI data," *IEEE Trans. Med. Imag.*, vol. 37, no. 2, pp. 547–556, Feb. 2018.

[6] H.-U. Kauczor *et al.*, "Imaging of the lungs using ^{3}He MRI: Preliminary clinical experience in 18 patients with and without lung disease," *J. Magn. Reson. Imag.*, vol. 7, no. 3, pp. 538–543, Jun. 1997.

[7] H. Marshall *et al.*, "Direct visualisation of collateral ventilation in COPD with hyperpolarised gas MRI," *Thorax*, vol. 67, no. 7, pp. 613–617, Jul. 2012.

[8] D. A. Roberts *et al.*, "Detection and localization of pulmonary air leaks using laser-polarized ^{3}He MRI," *Magn. Reson. Med.*, vol. 44, no. 3, pp. 379–382, Sep. 2000.

[9] J. M. Wild, F. C. Horn, G. J. Collier, and H. Marshall, "Dynamic imaging of lung ventilation and gas flow with hyperpolarized gas MRI," in *Hyperpolarized and Inert Gas MRI*, F. T. Hane, Ed. Boston, MA, USA: Academic, 2017, pp. 47–59.

[10] M. Viallon *et al.*, "Dynamic imaging of hyperpolarized ^{3}He distribution in rat lungs using interleaved-spiral scans," *NMR Biomed.*, vol. 13, no. 4, pp. 207–213, Jun. 2000.

[11] M. Salerno, T. A. Altes, J. R. Brookeman, E. E. de Lange, and J. P. Mugler, III, "Dynamic spiral MRI of pulmonary gas flow using hyperpolarized ^{3}He: Preliminary studies in healthy and diseased lungs," *Magn. Reson. Med.*, vol. 46, no. 4, pp. 667–677, Oct. 2001.

[12] D. Dupuich, Y. Berthezène, P. L. Clouet, V. Stupar, E. Canet, and Y. Crémillieux, "Dynamic ^{3}He imaging for quantification of regional lung ventilation parameters," *Magn. Reson. Med.*, vol. 50, no. 4, pp. 777–783, Oct. 2003.

[13] J. M. Wild *et al.*, "Dynamic radial projection MRI of inhaled hyperpolarized ^{3}He gas," *Magn. Reson. Med.*, vol. 49, no. 6, pp. 991–997, Jun. 2003.

[14] M. Lustig, D. Donoho, and J. M. Pauly, "Sparse MRI: The application of compressed sensing for rapid MR imaging," *Magn. Reson. Med.*, vol. 58, no. 6, pp. 1182–1195, 2007.

[15] S. Ravishankar and Y. Bresler, "MR image reconstruction from highly undersampled k-space data by dictionary learning," *IEEE Trans. Med. Imag.*, vol. 30, no. 5, pp. 1028–1041, May 2011.

[16] X. Qu *et al.*, "Undersampled MRI reconstruction with patch-based directional wavelets," *Magn. Reson. Imag.*, vol. 30, no. 7, pp. 964–977, Sep. 2012.

[17] S. G. Lingala and M. Jacob, "Blind compressive sensing dynamic MRI," *IEEE Trans. Med. Imag.*, vol. 32, no. 6, pp. 1132–1145, Jun. 2013.

[18] S. Wang *et al.*, "Learning joint-sparse codes for calibration-free parallel MR imaging," *IEEE Trans. Med. Imag.*, vol. 37, no. 1, pp. 251–261, Jan. 2018.

[19] S. Ajraoui, J. Parra-Robles, and J. M. Wild, "Incorporation of prior knowledge in compressed sensing for faster acquisition of hyperpolarized gas images," *Magn. Reson. Med.*, vol. 69, no. 2, pp. 360–369, Feb. 2013.

[20] Y. Pang and X. Zhang, "Interpolated Compressed Sensing for 2D Multiple Slice Fast MR Imaging," *PLoS ONE*, vol. 8, no. 2, p. e56098, Feb. 2013.

[21] C. Chen, Y. Li, L. Axel, and J. Huang, "Real time dynamic MRI by exploiting spatial and temporal sparsity," *Magn. Reson. Imag.*, vol. 34, no. 4, pp. 473–482, 2016.

[22] U. Nakarmi, Y. Wang, J. Lyu, D. Liang, and L. Ying, "A kernel-based low-rank (KLR) model for low-dimensional manifold recovery in highly accelerated dynamic MRI," *IEEE Trans. Med. Imaging*, vol. 36, no. 11, pp. 2297–2307, Nov. 2017.

[23] R. Otazo, E. Candès, and D. K. Sodickson, "Low-rank plus sparse matrix decomposition for accelerated dynamic MRI with separation of background and dynamic components," *Magn. Reson. Med.*, vol. 73, no. 3, pp. 1125–1136, 2015.

[24] S. Xiao *et al.*, "Considering low-rank, sparse and gas-inflow effects constraints for accelerated pulmonary dynamic hyperpolarized ^{129}Xe MRI," *J. Magn. Reson.*, vol. 290, pp. 29–37, May 2018.

[25] E. R. Weibel, "Geometric and dimensional airway models of conductive, transitory and respiratory zones of the human lung," in *Morphometry of the Human Lung*, E. R. Weibe, Ed. Boston, MA, USA: Academic, 1963, pp. 136–142.

[26] J. C. Woods and M. S. Conradi, "He-3 diffusion MRI in human lungs," *J. Magn. Reson.*, vol. 292, pp. 90–98, Jul. 2018.

[27] D. L. Donoho, "Compressed sensing," *IEEE Trans. Inf. Theory*, vol. 52, no. 4, pp. 1289–1306, Apr. 2006.

[28] E. J. Candés and T. Tao, "Near-optimal signal recovery from random projections: Universal encoding strategies," *IEEE Trans. Inf. Theory*, vol. 52, no. 12, pp. 5406–5425, Dec. 2006.

[29] E. J. Candès, J. Romberg, and T. Tao, "Robust uncertainty principles: Exact signal reconstruction from highly incomplete frequency information," *IEEE Trans. Inf. Theory*, vol. 52, no. 2, pp. 489–509, Feb. 2006.

[30] E. J. Candès and M. B. Wakin, "An introduction to compressive sampling," *IEEE Signal Process. Mag.*, vol. 25, no. 2, pp. 21–30, Mar. 2008.

[31] I. Daubechies, M. Defrise, and C. De Mol, "An iterative thresholding algorithm for linear inverse problems with a sparsity constraint," *Commun. Pure Appl. Math.*, vol. 57, no. 11, pp. 1413–1457, Nov. 2004.

[32] J. Yang and Y. Zhang, "Alternating direction algorithms for ℓ_1-problems in compressive sensing," *SIAM J. Sci. Comput.*, vol. 33, no. 1, pp. 250–278, Feb. 2011.

[33] Q. Liu, S. Wang, and D. Liang, "Sparse and dense hybrid representation via subspace modeling for dynamic MRI," *Comput. Med. Imag. Grap.*, vol. 56, pp. 24–37, Mar. 2017.

[34] N. Cai, S. Wang, S. Zhu, and D. Liang, "Accelerating dynamic cardiac MR imaging using structured sparse representation," *Comput. Math. Method. Med.*, vol. 2013, Nov. 2013, Art. no. 160139.

[35] X. J. Chen *et al.*, "MR microscopy of lung airways with hyperpolarized ^{3}He," *Magn. Reson. Med.*, vol. 39, no. 1, pp. 79–84, Jan. 1998.

[36] O. Doganay *et al.*, "Fast dynamic ventilation MRI of hyperpolarized ^{129}Xe using spiral imaging," *Magn. Reson. Med.*, vol. 79, no. 5, pp. 2597–2606, May 2018.

[37] S. Appelt, A. B.-A. Baranga, C. J. Erickson, M. V. Romalis, A. R. Young, and W. Happer, "Theory of spin-exchange optical pumping of ^{3}He and ^{129}Xe," *Phys. Rev. A, Gen. Phys.*, vol. 58, no. 2, pp. 1412–1439, Aug. 1998.

[38] Z. Wang, A. C. Bovik, H. R. Sheikh, and E. P. Simoncelli, "Image quality assessment: From error visibility to structural similarity," *IEEE Trans. Image Process.*, vol. 13, no. 4, pp. 600–612, Apr. 2004.

[39] S. Aja-Fernandez, R. S. J. Estepar, C. Alberola-Lopez, and C.-F. Westin, "Image quality assessment based on local variance," in *Proc. IEEE Int. Conf. Eng. Med. Biol. Soc.*, New York, NY, USA, Jul./Aug. 2006, pp. 4815–4818.

[40] A. Bruhn, J. Weickert, and C. Schnörr, "Lucas/Kanade meets horn/schunck: Combining local and global optic flow methods," *Int. J. Comput. Vis.*, vol. 61, no. 3, pp. 211–231, 2005.

[41] G. J. Collier and J. M. Wild, "*In vivo* measurement of gas flow in human airways with hyperpolarized gas MRI and compressed sensing," *Magn. Reson. Med.*, vol. 73, pp. 2255–2261, Jun. 2015.